Available online at www.sciencedirect.com
ScienceDirect
Trans. Nonferrous Met. Soc. China 35(2025) 2935−2953
Transactions of Nonferrous Metals Society of China
www.tnmsc.cn

Effect of cross-section change on microstructure and properties of quasi β forging of Ti-55511 alloy large-scale components

Heng-jun LUO[1,2], Hao DENG[2], Wu-hua YUAN[1], Wei XIANG[1,2], Chang-min LI[2], Wei-dong YIN[2], Hui YIN[2], Zou-yuan XU[2], Sheng CAO[3]

1. College of Materials Science and Engineering, Hunan University, Changsha 410082, China;
2. Deyang Wanhang Die Forging Co., Ltd., China National Erzhong Group Co., Deyang 618013, China;
3. Institute of Advanced Wear & Corrosion Resistant and Functional Materials, College of Chemistry and Materials Science, Jinan University, Guangzhou 510632, China

Received 16 January 2024; accepted 9 August 2024

Abstract: The microstructure and mechanical properties of the Ti−5Al−5Mo−5V−1Cr−1Fe (Ti-55511) alloy under different strains were investigated through the design of step-shaped die forging. The results indicate that continuous dynamic recrystallization (CDRX) and discontinuous dynamic recrystallization (DDRX) occur in the high strain region. The orientation of the grains produced by CDRX is random and does not weaken the fiber texture. ⟨100⟩-oriented grains expand gradually with increasing strain, thereby enhancing the strength of {100} texture. Significant anisotropic mechanical properties are observed in the large strain region and analyzed through in-situ tensile experiments. When the loading direction is parallel to the longitudinal (L) direction, strain concentration is observed near the dynamically recrystallized (DRXed) grains and inside grains oriented along ⟨100⟩, leading to crack initiation. Furthermore, the small angle between the loading direction and the *c*-axis hinders the activation of prismatic and basal slip, thereby enhancing the strength. When the loading direction is parallel to the short transverse (ST) direction, cracks are initiated not only within grains oriented along ⟨100⟩, but also at the grain boundaries. Regarding impact toughness, the elongated β grains in the L direction enhance the resistance to crack propagation.

Key words: Ti−5Al−5Mo−5V−1Cr−1Fe alloy; step-shaped die forgings; strain distribution; deformation mechanism; mechanical properties

1 Introduction

Ti−5Al−5Mo−5V−1Cr−1Fe (Ti-55511) is a typical near β titanium alloy widely utilized in the aviation industry for load-bearing components due to its outstanding mechanical properties and corrosion resistance [1,2]. Generally, thermo-mechanical processing (TMP) is employed in the manufacturing of β titanium alloy load-bearing components. This process includes hot deformation in the β region or α+β region, followed by specific heat treatment strategies to control the microstructure of the die forgings and release residual stress [3,4]. These processes are designed to achieve microstructures and mechanical properties that meet the standards required for aerospace applications [5].

Numerous studies have investigated small-sized Ti-55511 samples prepared by TMP, focusing on hot deformation behavior [6−9], microstructure, and texture evolution [10−13]. LIANG et al [7,8] conducted Gleeble experiments to study the hot deformation behavior of Ti-55511 alloy in the α+β

Corresponding author: Wu-hua YUAN, Tel: +86-13875808653, E-mail: yuan46302@163.com
https://doi.org/10.1016/S1003-6326(25)66858-0

region and β region and established constitutive models to describe the dynamic recovery (DRV) and dynamic recrystallization (DRX) processes of Ti-55511 alloy. LIM et al [12] and LI and YANG [10] investigated the texture evolution of Ti-55511 alloy during hot deformation in the β phase region, which revealed the influence of dynamic strain-induced boundary migration on the formation of {111} and {100} textures. Other studies have demonstrated that the microstructure of Ti-55511 alloy after forging can be controlled through heat treatment. These studies also aimed to establish the relationship of heat treatment parameters, microstructure variations, and resulting mechanical properties. SHI et al [14,15] established a fracture toughness prediction model to study the influence of heat treatment on the evolution of basket-weave microstructure in Ti55511 alloy and elucidated the crack initiation mechanism under high-cycle fatigue. BOYER [16] established the relationship between the microstructures and dynamic behaviors in Ti55511 alloys with bimodal, equiaxed, basket-weave, and Widmanstatten microstructures [1].

Note that the aforementioned studies were conducted in laboratory settings using small specimens and carefully controlled processing conditions. In aviation applications, large die forgings are the predominant form of titanium alloys utilized, typically fabricated through die forging processes that employ molds to shape alloy blanks into specific configurations [16]. Die forging is favored for aerospace titanium alloys due to its advantages, such as no material limitations, excellent surface finish, and the ability to control microstructure. It is considered one of the most reliable manufacturing methods [17−19]. GUPTA et al [20] studied the microstructure and tensile performance of Ti−6Al−4V pressure vessel die forgings in different regions and discussed the variants of thermomechanical processing along with annealing to achieve better uniformity in properties and microstructure. SUÁREZ FERNÁNDEZ et al [21] explored the effect of forging texture and machining parameters on the fatigue performance of Ti−6Al−2Sn−4Zr−6Mo large-scale die forged discs, revealing the formation mechanisms of texture at different locations and their influence on the fatigue performance.

Currently, some studies have begun to scale up the size of parts. However, in actual industrial production, the complex cross-sectional changes of large die forgings present significant challenges. Conventional part design often struggles to effectively guide the forging production process. At identical deformation temperatures and speeds, the strain distribution within the parts varies significantly, thereby influencing the uniformity of microstructure and properties across the forgings. In other words, die forgings with complex geometries often exhibit varying thicknesses across a single forging. Therefore, it is crucial to analyze how strain distribution at different positions during the forging process of large die forgings impacts microstructure and mechanical properties.

In this study, the microstructure, deformation mechanisms, texture evolution, and mechanical properties of Ti-55511 alloy were investigated across various strain levels using step-shaped die forging. The in-situ tensile process was analyzed under different loading directions. The influence of DRX behavior on texture was discussed, revealing the reasons for the variations in mechanical properties within the large strain regions. The findings of this study offer theoretical support for the engineering applications of large-sized Ti 55511 alloy die forgings fabricated through TMP.

2 Experimental

2.1 Raw material

The Ti-55511 alloy pre-form billet was produced by Hunan Xiangtou Goldsky New Materials Co., Ltd. The chemical composition of the Ti-55511 alloy was determined at Ti−5.20Al−4.95Mo−4.96V−1.05Cr−0.95Fe−0.18O−0.005N (wt.%). The β transus temperature (T_β) was determined at 875 °C by the metallographic method [22]. The size of the pre-form billet was 165 mm × 165 mm × 520 mm (Fig. 1(a)). The microstructure of the initial billet, which has a typical bi-modal microstructure, is presented in Fig. 1(b).

2.2 Die forging and heat treatment process

A step-shaped die forging was designed to obtain various deformation reductions, as shown in Fig. 1. The billet size was 520 mm × 165 mm, and the initial microstructures are shown in Figs. 1(a) and (b). The thicknesses of the four positions of the die forgings were 135, 120, 100, and 80 mm, denoted as S1, S2, S3, and S4, respectively, as

shown in Fig. 1(c). The dies were made of H13 steel. Before the die forging process, the billet was soaked at 905 °C for 2.5 h. Subsequently, the Ti-55511 billet was transferred to a die forging press with a transfer time within 30 s. After the die forging process, the Ti-55511 die forgings were air-cooled (AC) to room temperature, as shown in Fig. 1(d).

Subsequently, the forgings were double annealed to obtain the basket-weave microstructure, as shown in Fig. 2(a). In detail, the as-forged Ti-55511 component was heat treated at 850 °C for 2 h, and then furnace cooled (FC) to 740 °C for 2 h, followed by AC. The ageing process was performed at 600 °C for 8 h.

2.3 Finite element modeling

The die forging process was simulated using the rigid-plastic finite element program DEFORM-3D™. The Ti-55511 workpiece and AISI H13 dies were defined as plastic and rigid bodies with 30000 and 10000 quadrilateral finite element meshes, respectively. Furthermore, a shear friction model was chosen to simulate frictional behaviors during the hot die forging process. The thermo-physical parameters (such as flow stresses, thermal conductivity, and heat transfer coefficient) of Ti-55511 and H13 were set according to the database of the Deform software.

2.4 Microstructure characterization

An FEI Inspect F50 field-emission scanning electron microscope (SEM) equipped with an electron backscattered diffraction (EBSD) detector (NordlysNano, Oxford) was used for the microstructure analysis and grain orientation characterization.

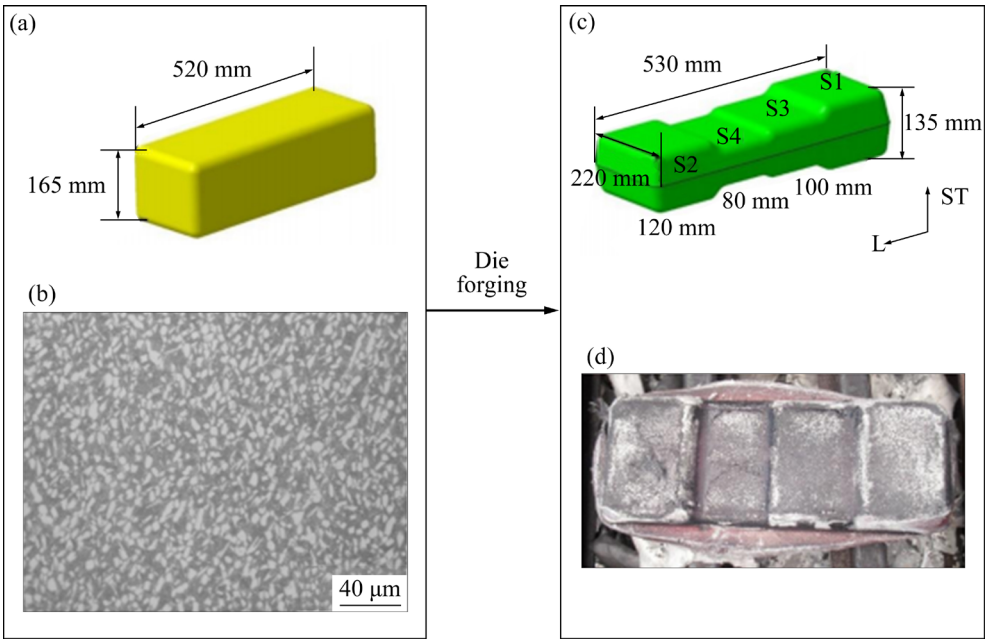

Fig. 1 (a) Original billet size of Ti-55511 alloy; (b) Initial microstructure of Ti-55511 billet in (a); (c) Thicknesses of four positions of die forgings; (d) Illustration of Ti-55511 alloy die forgings (L−Longitudinal direction; ST−Short transverse direction)

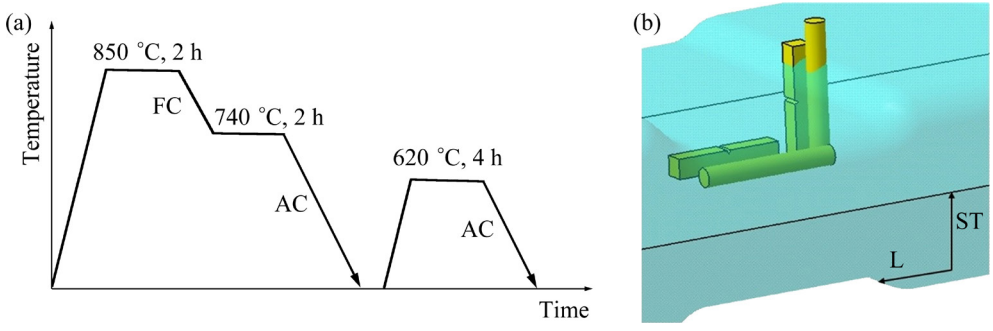

Fig. 2 Illustration of double annealing (a), and mechanical testing samples sectioned from die forgings (b)

SEM samples were ground using SiC paper to #2500 finish and then etched using Kroll's agent (1 vol.% HF + 4 vol.% HNO_3 + 95 vol.% H_2O). EBSD samples were polished using a vibration polisher (Buehler VibroMet 2). Channel 5 software was used for EBSD data processing. Quantitative microstructure analyses were carried out by using Image Pro Plus software.

2.5 Mechanical properties tests

Standard cylindrical tension test samples with a diameter of 5 mm were used for the tensile tests, according to the ASTM E8/E8M-16a standard, as shown in Fig. 3(a). The ultimate tensile strength (UTS), yield strength (YS), and elongation (El) were obtained on an Instron 8801 machine equipped with an extensometer. The tensile strain rate was 0.5 mm/min. Impact toughness tests were conducted on an Instron MPX machine using U-notch specimens, according to GB/T 229—2007. In this study, mechanical test samples were extracted from two directions to explore the mechanical properties of die forgings in different orientations. Specifically, the L direction was perpendicular to the forging direction, and the ST direction was parallel to the forging direction, as illustrated in Fig. 2(b).

The in-situ tensile test was carried out by a scanning electron microscope with a loading stage and EBSD. First, two groups of samples were cut by wire cutting at the same position of the forging, with the sample sizes shown in Fig. 3(b). Subsequently, the samples underwent mechanical grinding and electrolytic polishing. In the testing phase, the first group underwent a tensile test outside the sample chamber to determine the stress and strain range of the samples, which served as the basis for selecting the samples for the tensile test inside the chamber. Subsequently, the tensile test was conducted inside the sample chamber. When the load reached a certain strain level, the loading was paused, and an EBSD test was conducted. After completing the test, loading resumed, and the test was repeated at the same position until the sample fractured.

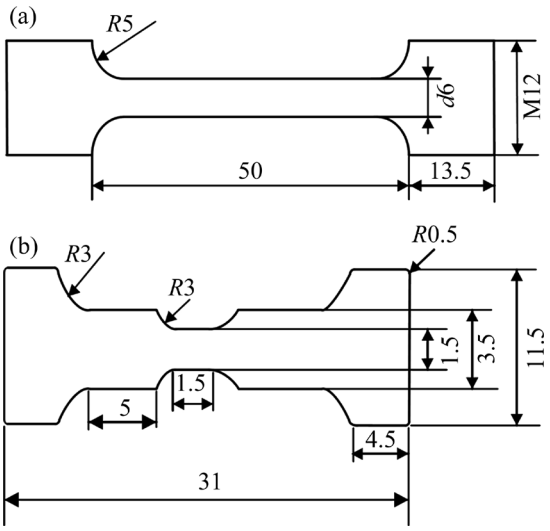

Fig. 3 (a) Geometric shape and size of tensile specimen; (b) Geometric shape and size of in-situ tensile specimen (Unit: mm)

3 Results

3.1 Strain distribution of step-shaped die forgings

Deform-3D finite element analysis was used to analyze the effective strain during the die forging deformation process, and the corresponding results are shown in Fig. 4. The strain distribution across the die forgings indicates effective strains in regions S1 to S4 as 0.375−0.500, 0.500−0.625, 0.625−0.750, and 0.750−1.000, respectively. This is attributed to the significant deformation that occurs to the billet (165 mm × 165 mm), which is deformed from 165 to 100 mm (S3) and 80 mm (S4). Consequently, relatively high effective strains are observed in these regions. On the other hand, the forging thickness of S1 and S2 is greater (135 mm and 120 mm, respectively), leading to lower deformation during the die forging process. Therefore, the effective strain is smaller than that of S3 and S4. Table 1 presents the simulation results for the effective strain in Regions S1, S2, S3 and S4. Due to the effective strain distribution ranging from 0.375 to 1 in the central regions of all four steps of the die forgings, further research will focus on studying the microstructure and mechanical properties of these typical regions in subsequent investigations.

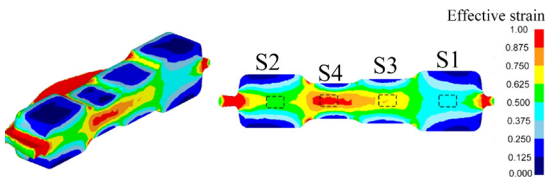

Fig. 4 Strain distribution of Ti-55511 alloy die forgings

Table 1 Simulation results of effective strain with respect to Ti-55511 die forgings

Sample	Thickness/mm	Effective strain
S1	135	0.375−0.500
S2	120	0.500−0.625
S3	100	0.625−0.750
S4	80	0.750−1.000

3.2 Microstructure and texture of die forgings

Given the strain ranging from 0.25 to 1.00, EBSD characterizations were conducted on four core regions. Figure 5 shows the EBSD results of different locations. Figure 6 illustrates the distribution of grain boundaries at different locations. In the S1 sample position (strain range of 0.375−0.500), the β grains exhibit an elongated morphology, indicating that the primary deformation mechanism at this stage is DRV, as depicted in Fig. 5(a). The proportion of low angle grain boundaries (LAGBs) is 65.35% (Fig. 6(a)). The DRV process promotes the formation of low-angle grain boundaries (LAGBs) through dislocation arrangements and continuously increases misorientation by absorbing dislocations [23]. It can be observed from the kernel average misorientation (KAM) map that dislocations are predominantly concentrated near the grain boundaries (Fig. 5(c)). A KAM map serves to visualize the strain distribution [24]. As the strain increases to 0.500−0.625 in the S2 sample, numerous small dynamically recrystallized (DRXed)

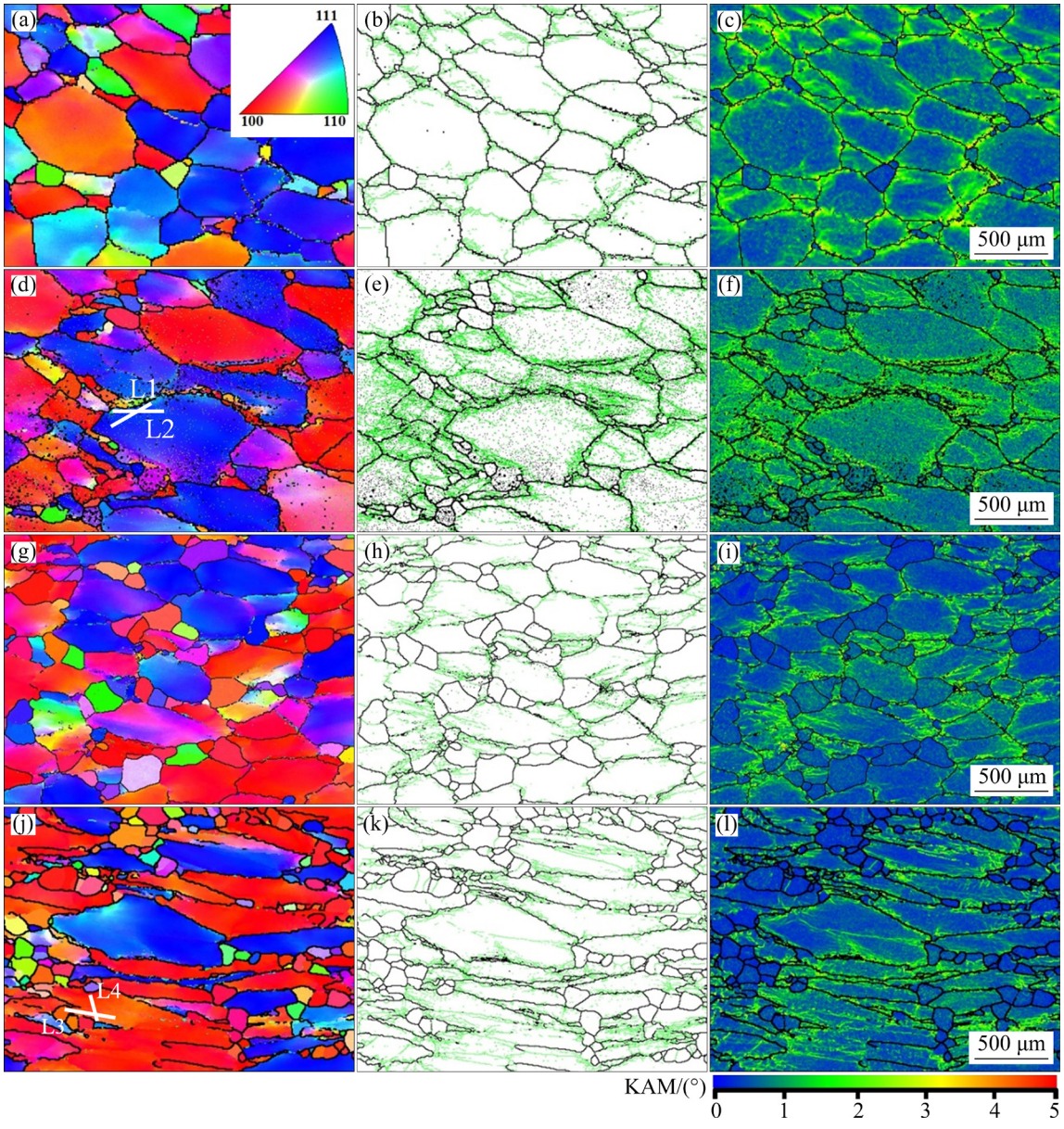

Fig. 5 IPF maps (a, d, g, j), GBs maps (b, e, h, k), and KAM maps (c, f, i, l): (a−c) S1; (d−f) S2; (g−i) S3; (j−l) S4

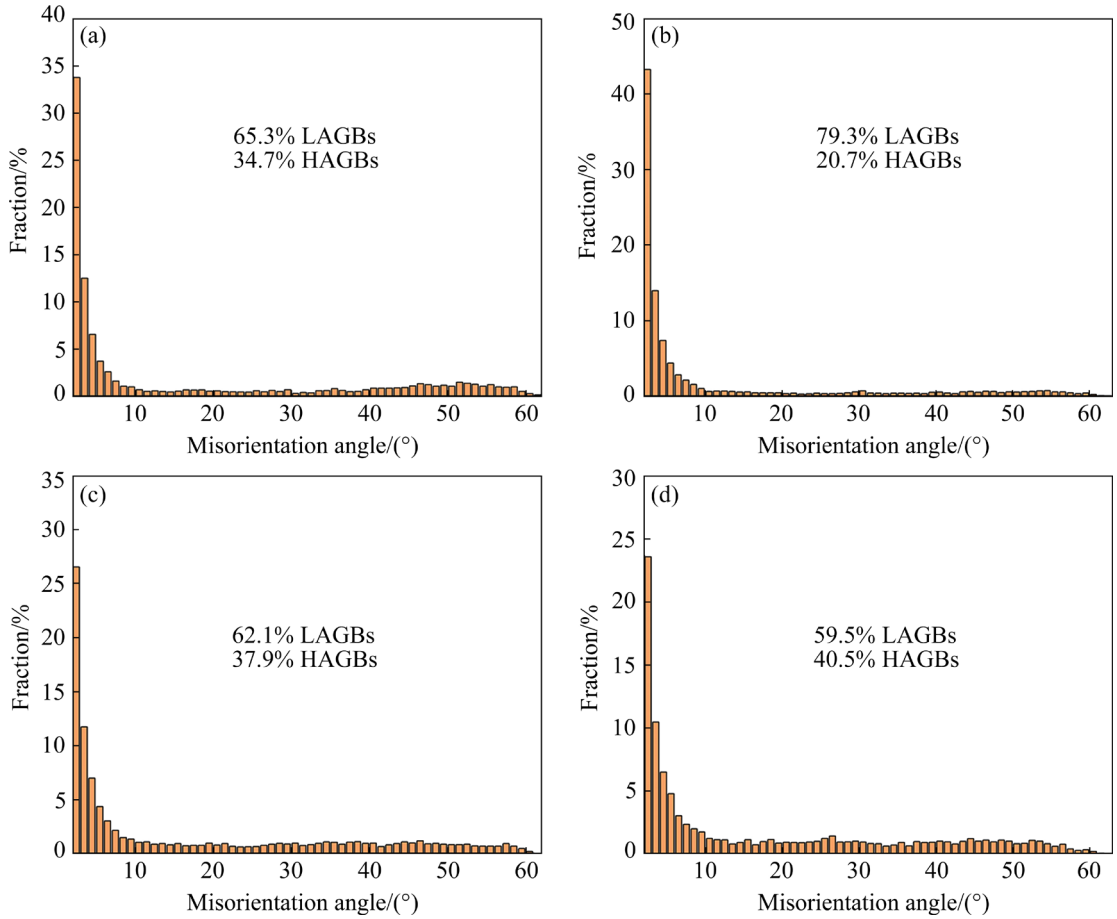

Fig. 6 Grain boundary distribution maps in different strain regions: (a) S1; (b) S2; (c) S3; (d) S4

grains generate near the prior β grains (Fig. 5(d)). At this stage, the proportion of LAGBs increases to 79.3% (Fig. 6(b)), indicating that DRV remains the primary deformation mechanism. It should be noted that a significant number of LAGBs provide ample driving energy for the nucleation and growth of subsequent DRX. In the S3 region, numerous DRXed grains can be observed in Fig. 5(g). In the S4 region, the prior β grains further elongate under large strain, and the proportion of LAGBs decreases to 59.5% (Fig. 6(d)). Concurrently, the dislocation density also exhibits a significant decrease (Fig. 5(l)). This indicates that LAGBs gradually absorb dislocations and transform into DRXed grains with HAGBs during the deformation process. Additionally, it can be observed that the dislocation density in DRXed grains is very low (Figs. 5(i, l)).

Figure 7 shows the inverse pole figures (IPFs) of the S1−S4 regions and reflects the texture conditions. Figures 7(a) and (b) indicate that the IPFs of the S1 and S2 samples exhibit a random distribution of β grains without any significant preferred orientation. It confirms that the strain range of 0.375−0.625 in the die forging process of Ti-55511 alloy does not induce β texture. It should be pointed out that in the S2 region, the grains have already deviated towards the ⟨100⟩ and ⟨111⟩ directions. However, when the strain increases to 0.625−0.750, the S3 sample shows a mixed ⟨111⟩ and ⟨100⟩ fiber texture along the ST direction, as shown in Fig. 7(c). Figure 7(d) illustrates that as the strain increases to 0.750−1.000, a large number of {100} oriented grains are formed (see Fig. 5(j)). The volume fraction of β texture for positions S1−S4 was further analyzed using Channel 5 software, and the results are shown in Fig. 8. The statistical analysis indicates a trend of increasing volume fractions of ⟨111⟩-oriented grains at S1−S4 positions, namely 21.2% (S1), 26.5% (S2), 38.5% (S3), and 40.2% (S4). Additionally, the volume fractions of ⟨100⟩-oriented grains significantly increase when the strain exceeds 0.625−0.750. Specifically, the volume fraction of ⟨100⟩-oriented grains increases from 21.2% at S2 to 49.6% at S3,

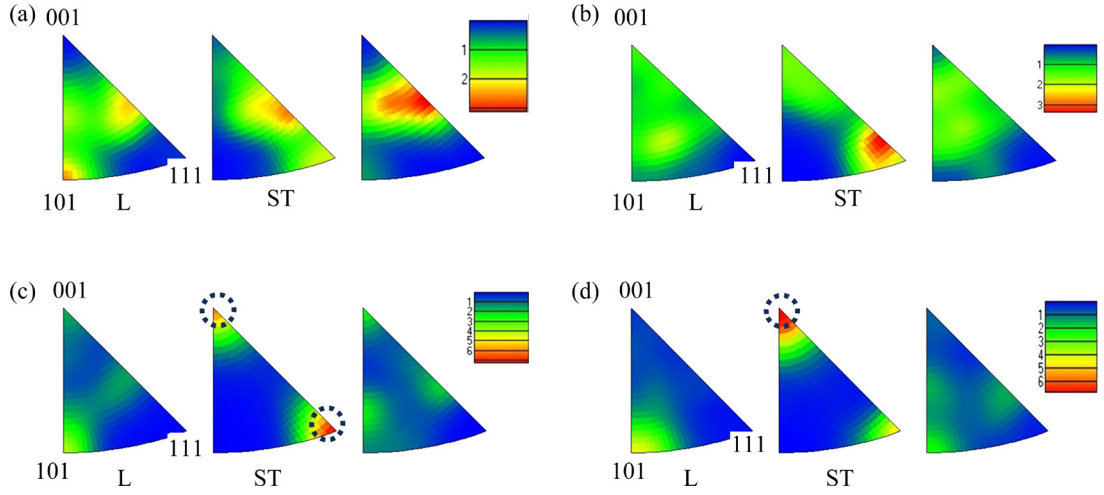

Fig. 7 IPF maps from Fig. 4 of S1 (a), S2 (b), S3 (c) and S4 (d)

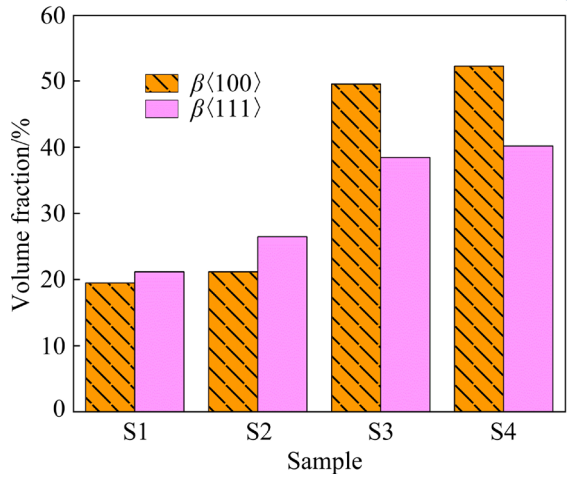

Fig. 8 Volume fractions of ⟨100⟩ and ⟨111⟩ texture

with sample S4 showing the largest volume fraction among the four positions, reaching 52.3%. These results indicate that during the β forging process, the ⟨100⟩ texture parallel to the ST direction gradually becomes the dominant deformation texture as the deformation reduction increases.

3.3 Microstructure of die forgings after heat treatment

Figure 9 shows the SEM images of the heat treated Ti-55511 alloy die forgings. After double annealing, the Ti-55511 alloy die forgings exhibit a typical basket-weave microstructure composed of lamellar primary α (α_p) and transformed β structure (β_{trans}). Table 2 presents the volume fractions of α_p in the S1−S4 samples, which are 32.5%, 32.8%, 33.5%, and 33.9%, respectively, with average widths of 1.64, 1.79, 1.65, and 1.73 μm. Statistical analysis revealed that there was no significant difference in the volume fraction and width of α_p lamellae for S1−S4 samples after heat treatment. This uniformity can be attributed to the consistent composition of all Ti-55511 billets, ensuring consistent diffusion kinetics of phase transformation at different strains in the die forgings. Furthermore, the double annealing heat treatment employed in this study involves a dwell stage at 850 °C for the nucleation and growth of α_p, followed by furnace cooling to 740 °C and subsequent dwell at 740 °C, facilitating the occurrence of diffusion-controlled $\beta \rightarrow \alpha$ phase transformation. As a result, the precipitation of α_p at different strain locations reaches an equilibrium state, leading to a relatively unchanged volume fraction and width of α_p. SEM was employed to investigate the precipitation of secondary α (α_s) in Ti-55511, as depicted in Fig. 10. Figure 10 demonstrates that the evolution of α_s shows no significant difference with increasing strain.

3.4 Mechanical properties in different strain regions

Table 3 lists the mechanical properties of the samples S1−S4 in different directions. For S1, the UTS and El in the L and ST directions are (1103±6) MPa, (1106±4) MPa, (16.0±0.5)%, and (13.5±0.3)%, respectively. However, for the higher strain S4 sample, the UTS noticeably decreases to (1088±6) MPa (L) and (1073±10) MPa (ST). Therefore, Table 3 illustrates that as strain increases, the mechanical properties of samples from the same location show significant differences in different directions. For the S1 and S2 samples, there are no

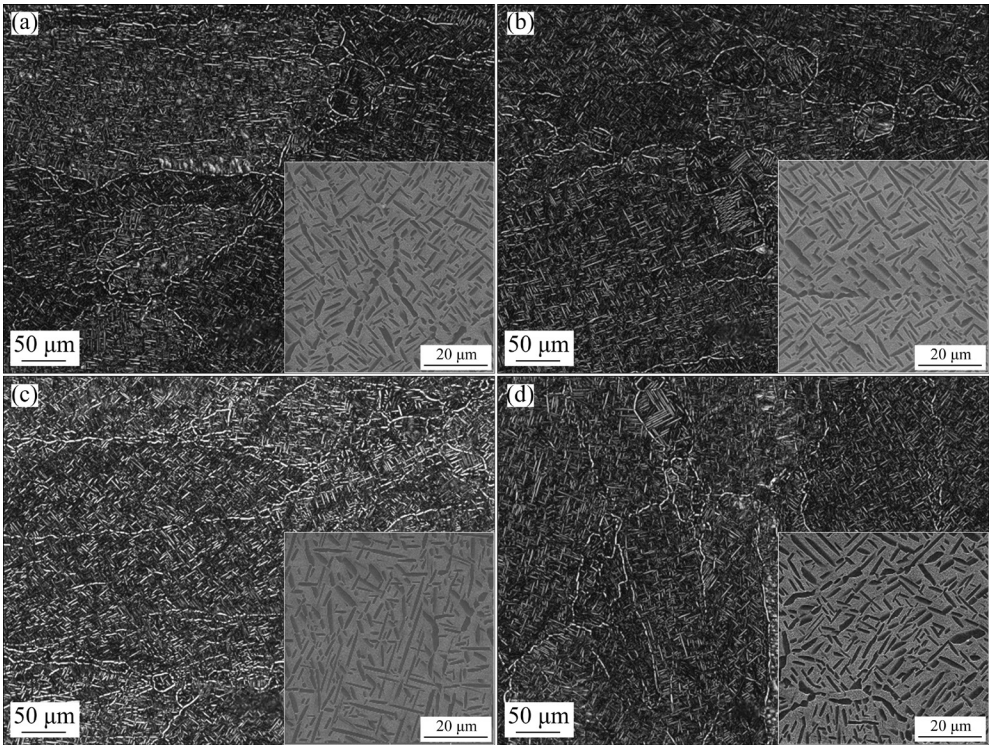

Fig. 9 SEM images of samples after heat treatment: (a) S1; (b) S2; (c) S3; (d) S4

Table 2 Thickness and volume fraction of α_p phase in S1−S4 region of Ti-55511 titanium alloy die forgings after double annealing

Sample	Thickness of α_p/μm	Volume fraction of α_p/%
S1	1.64	32.5
S2	1.79	32.8
S3	1.65	33.5
S4	1.73	33.9

significant differences in strength between the L and ST directions. However, the elongation and impact toughness in the ST direction are markedly reduced compared to those in the L direction. This trend is also evident in S3 and S4. Furthermore, as strain increases, there is a significant decrease in the UTS and YS at the S1−S4 locations. Table 2 indicates that the volume fraction and size of α_p remain nearly unchanged in different regions. Therefore, the variations in strength and elongation are primarily attributed to the morphology and texture of β grains.

3.5 In-situ tensile experiments in different directions

The stress−strain curves from in-situ tension are depicted in Fig. 11. After surpassing the yield point, three positions (P1, P2, P3) were selected to halt loading for subsequent EBSD testing. The in-situ tensile mechanical properties are shown in Table 4. Similar to Table 3, the anisotropy of mechanical properties in L and ST directions still exist. Figure 12 shows the EBSD results of different strain positions in the L direction. In the initial stage of tensile deformation (P1), strain mainly concentrates near the prior β grain boundary, with no significant deformation observed inside the grains (Fig. 12(a)) as a result of the presence of soft grain boundary α grains and associate precipitation -free zone (Fig. 9). The white box region in Fig. 12(a) is finely scanned, and the reconstruction information of the relevant region is depicted in Fig. 12(b). The reconstruction reveals the presence of two prior β grains with ⟨100⟩ orientation in this area, along with some equiaxed DRXed grains nearby. In the P2 stage, cracks begin to initiate. The black noises in Figs. 12(c) and (d) are microcracks. Combined with the KAM map and the reconstruction map of the P2 stage, it can be determined that the strain is mainly concentrated near the DRXed grains and inside the grains with ⟨100⟩ orientation. Moreover, cracks preferentially initiate in the vicinity of the fine DRXed grains. In the P3 stage, macroscopic cracks have appeared

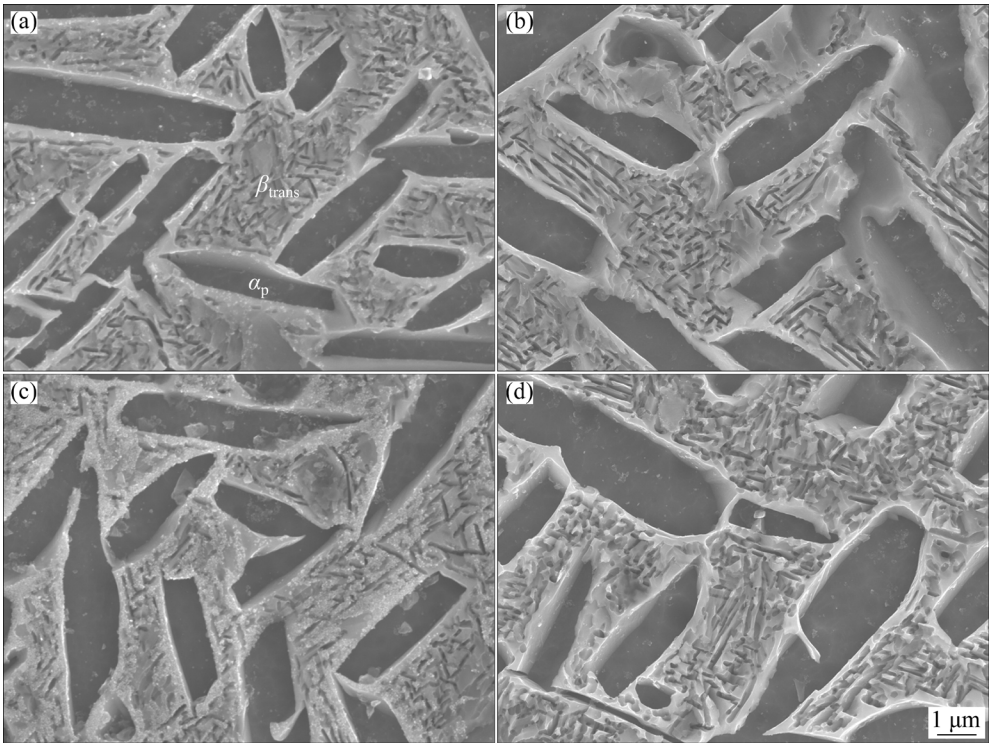

Fig. 10 SEM images showing β_{trans} microstructures of S1 (a), S2 (b), S3 (c), and S4 (d)

Table 3 Results of tensile and impact toughness tests

Sample	Direction	UTS/MPa	YS/MPa	El/%	Impact toughness/(kJ·m^{-2})
S1	L	1103±6	1028±8	16.0±0.5	495±15
	ST	1106±4	1036±10	13.5±0.3	351±10
S2	L	1105±11	1030±10	16.0±0.6	510±8
	ST	1096±9	1032±13	12.9±1.1	346±7
S3	L	1095±7	1020±5	15.4±1.3	552±13
	ST	1083±13	1020±7	11.8±0.7	308±9
S4	L	1088±6	1012±9	15.1±1.6	620±12
	ST	1073±10	1010±11	11.2±0.3	300±7

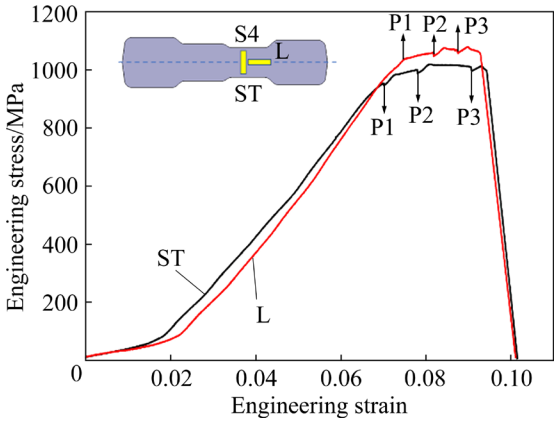

Fig. 11 Engineering stress−strain curves of Ti-55511 titanium alloy obtained in in-situ tensile test

near the DRXed grains, accompanied by numerous microcracks occurring within the grains oriented along ⟨100⟩, as depicted in Figs. 12(e) and (f).

Figure 13 shows the EBSD results at different strains (P1−P3 in Fig. 11) in the ST direction. During the initial stage of tensile deformation (P1), the strain was predominantly concentrated at the prior β grain boundary (Fig. 13(a)). At the P2 stage, the strain was highly localized within the ⟨100⟩ oriented grains, indicated by a relatively high degree of deformation. As deformation increases, crack initiation occurs at the grain boundaries of ⟨100⟩ oriented grains compared to the L direction, as indicated by the white arrows in Fig. 13(f). Therefore, when the loading direction is parallel to the ST direction, the crack occurs not only in the interior of the grain with ⟨100⟩ orientation but also at the grain boundary.

4 Discussion

4.1 Dynamic recrystallization behavior

Based on the previous results, it is evident that DRX becomes more pronounced as strain increases. To analyze the DRX behavior in different strain

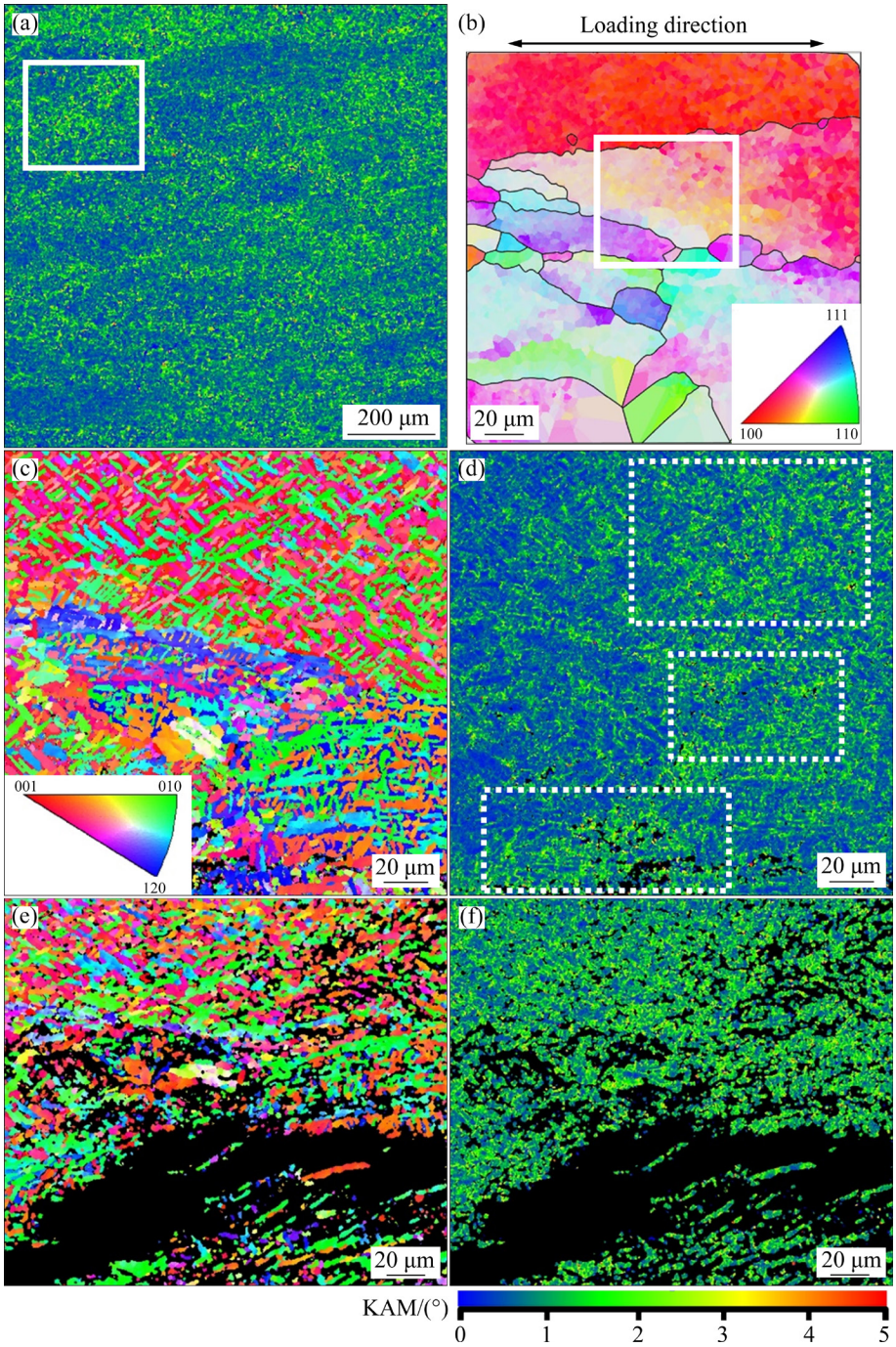

Fig. 12 EBSD results of different strains (P1−P3 in Fig. 11) in ST direction: (a) KAM map collected at P1; (b) Reconstructed prior β grains in fine scanning region; (c, d) IPF and associated KAM map collected at P2, respectively; (e, f) IPF and KAM map obtained at P3, respectively

Table 4 UTS and YS of TI-55511 in L and ST directions

Loading direction	UTS/MPa	YS/MPa
L	1075	1035
ST	1025	945

regions, this study first examined the DRX mechanism. The change in misorientation at the arrow in Fig. 5 is statistically analyzed, as shown in Fig. 14. From Figs. 14(a, b), it is evident that the cumulative misorientation increases gradually in the small strain region. However, the point-to-point misorientation remains less than 2°, suggesting a significant strain gradient within the prior β grain. This gradient creates favorable conditions for continuous dynamic recrystallization (CDRX). In the high strain region, the cumulative misorientation

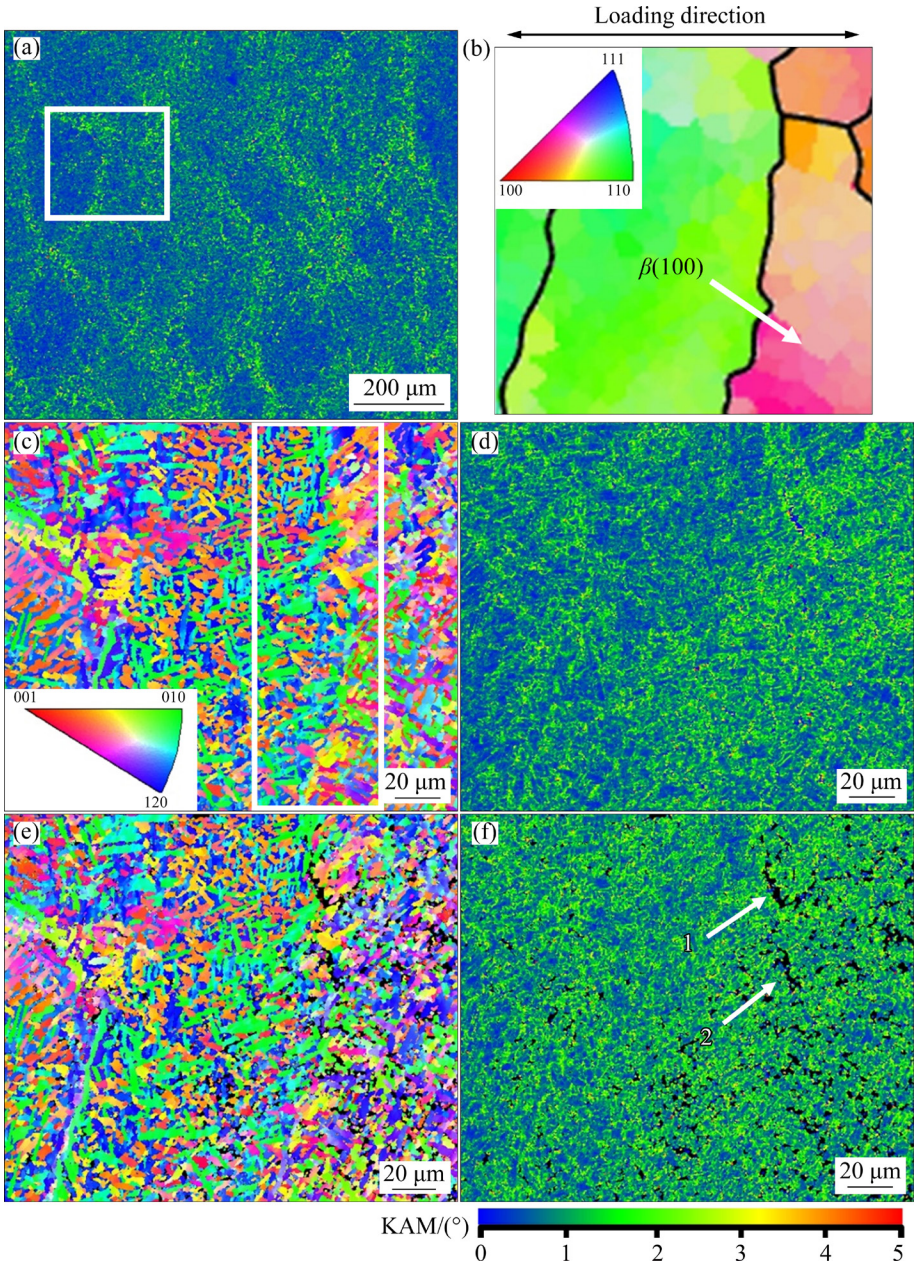

Fig. 13 EBSD results of different strains (P1−P3 in Fig. 11) in ST direction: (a) KAM map collected at P1; (b) Reconstructed prior β grains in fine scanning region; (c, d) IPF and associated KAM map collected at P2, respectively; (e, f) IPF and KAM map obtained at P3, respectively

continues to increase, with several peaks exceeding 2° observed in the point-to-point misorientation (Figs. 14(c, d)). This indicates the formation of LAGBs and the onset of subgrain progressive rotation processes. According to previous studies [25−28], cumulative misorientations exceeding 15° are considered characteristic of CDRX. It is worth noting that Fig. 5 also exhibits grain boundary bulging phenomena, which are indicative of discontinuous dynamic recrystallization (DDRX) [29,30].

In summary, based on the changing trend of misorientation, it can be concluded that DRV is the primary deformation mechanism in the small strain region, while CDRX predominates in the high strain region. Additionally, DDRX occurs concurrently. Figure 15 shows the DRX maps in different strain regions. In the figure, red represents deformed grains, yellow indicates substructured grains, and blue denotes DRXed grains. The volume fractions DRX in different regions are 4%, 6.28%, 20.84%, and 21.46%, respectively. The

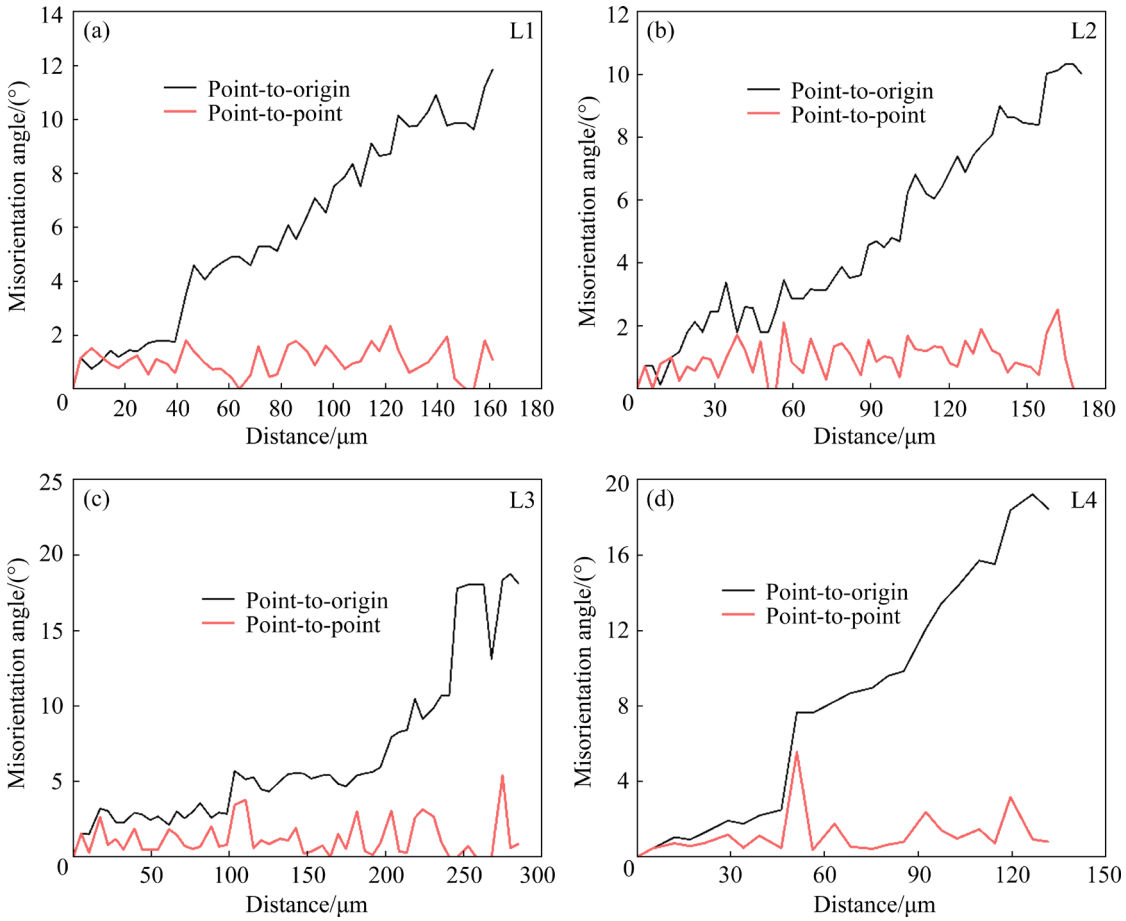

Fig. 14 Misorientation changes along arrows L1−L4 in Fig. 5

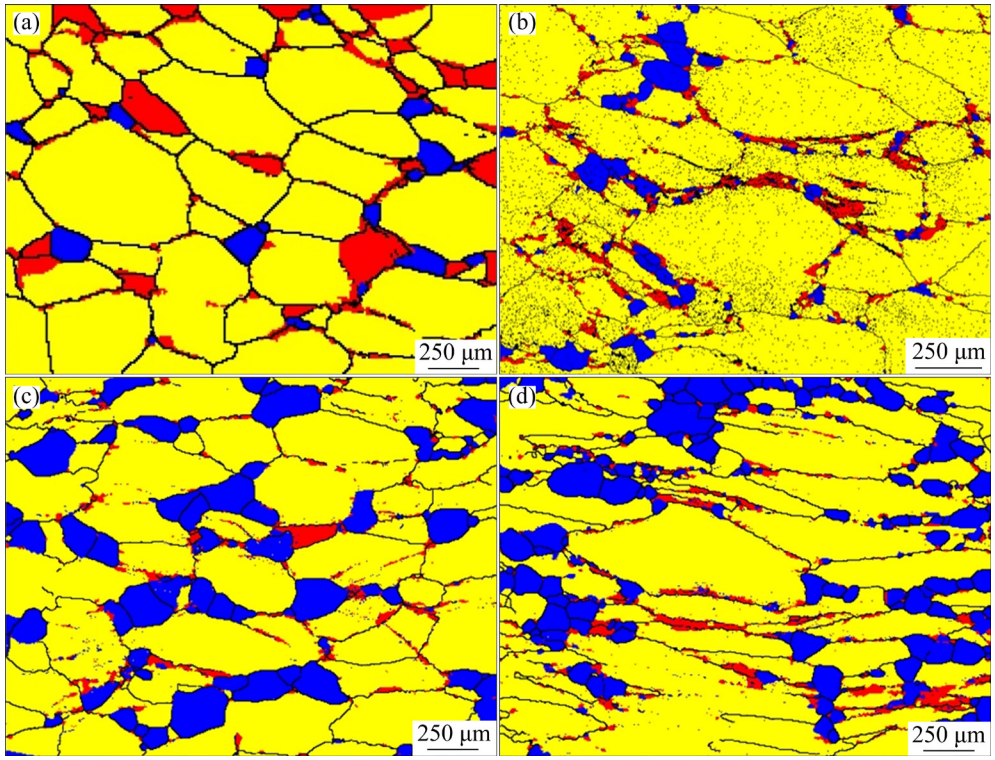

Fig. 15 DRX volume fraction in different strain regions: (a) S1; (b) S2; (c) S3; (d) S4

larger strain increases dislocation density, providing sufficient energy for DRX. As the volume fraction of DRX increases, dislocation density decreases significantly (Fig. 5). However, in the S3 and S4 regions, the volume fraction of DRX does not change significantly with increasing strain. The strain increase does not lead to a notable increase in the volume fraction of DRX. This observation may explain why the {100} texture intensity in the S4 region is higher than that in the S3 region. On the one hand, since titanium alloy is a high stacking fault metal, and CDRX can be regarded as a strong DRV mechanism, although the volume fraction can be increased, the DRV will also consume a large amount of deformation storage energy, which limits the increase in volume fraction of DRX. This underscores the critical role of DRV in the CDRX process [31]. On the other hand, by examining the orientation relationship between DRXed grains and unrecrystallized grains, it is evident that the orientation of DRXed grains is very random, as shown in Fig. 16. This phenomenon has also been reported by LI et al [32] and ZHANG et al [33]. Therefore, it is difficult to weaken the deformation texture by CDRX.

PRIMIG et al [34] believe that the Taylor factor of ⟨111⟩-oriented grains is greater than that of ⟨100⟩-oriented grains when {101} and {112} slip systems are taken into account for the calculation in a body-centered cubic structure. Therefore, ⟨111⟩-oriented grains possess higher stored energy during compression. This energy provides sufficient driving force for grain boundary migration from ⟨100⟩-oriented grains to ⟨111⟩-oriented grains, leading to gradual expansion of the ⟨100⟩-oriented grains and increasing the intensity of the {100} texture. Furthermore, LIM et al [12] observed that the grain boundaries of the near ⟨001⟩ oriented grains exhibit a higher misorientation towards ⟨111⟩-oriented grains, causing the ⟨001⟩ recrystallized grains to grow towards the deformed ⟨111⟩ grains, consuming some of the ⟨111⟩ oriented grains. Similar studies have been reported in the Ref. [10]. In summary, DRV, CDRX and DDRX collectively influence the strength of the texture during the deformation process.

4.2 Impact of β texture on α phase precipitation

Figure 7 indicates strong ⟨100⟩ and ⟨111⟩ textures in the S3 and S4 samples. Previous studies have suggested that the texture of the prior β phase may influence the orientation during the precipitation of the α phase. In order to explore the influence of β phase texture on α phase precipitation, an EBSD analysis was performed on the S4 sample and the results are shown in Fig. 17. Figure 17(a) represents the grain orientation distribution maps of the S4 sample, with grains

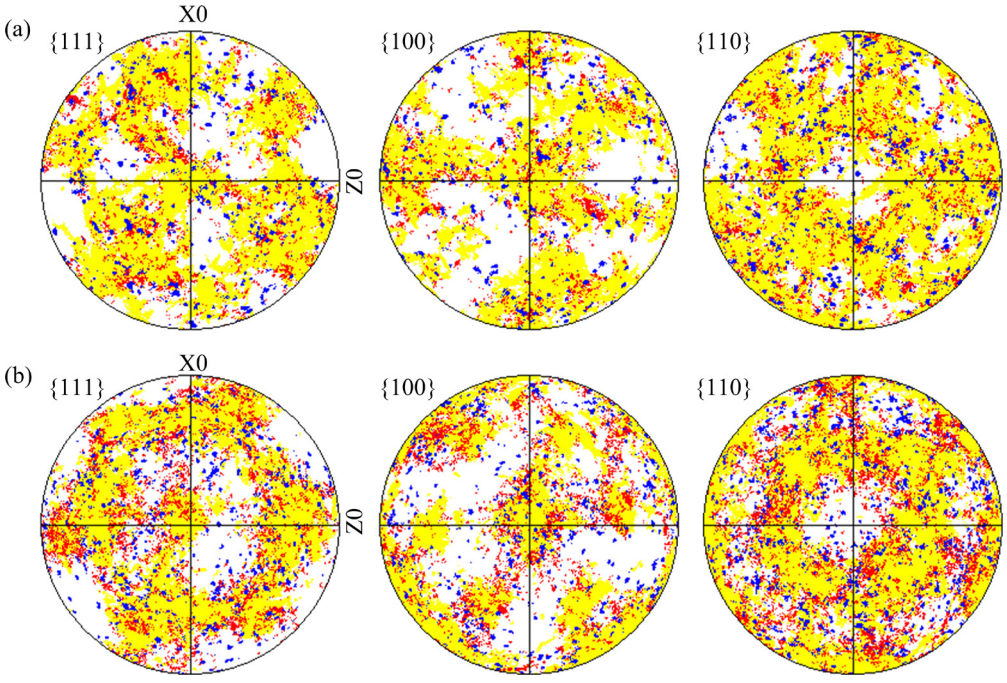

Fig. 16 Orientation relationship of DRXed grains in S3 (a) and S4 (b) regions

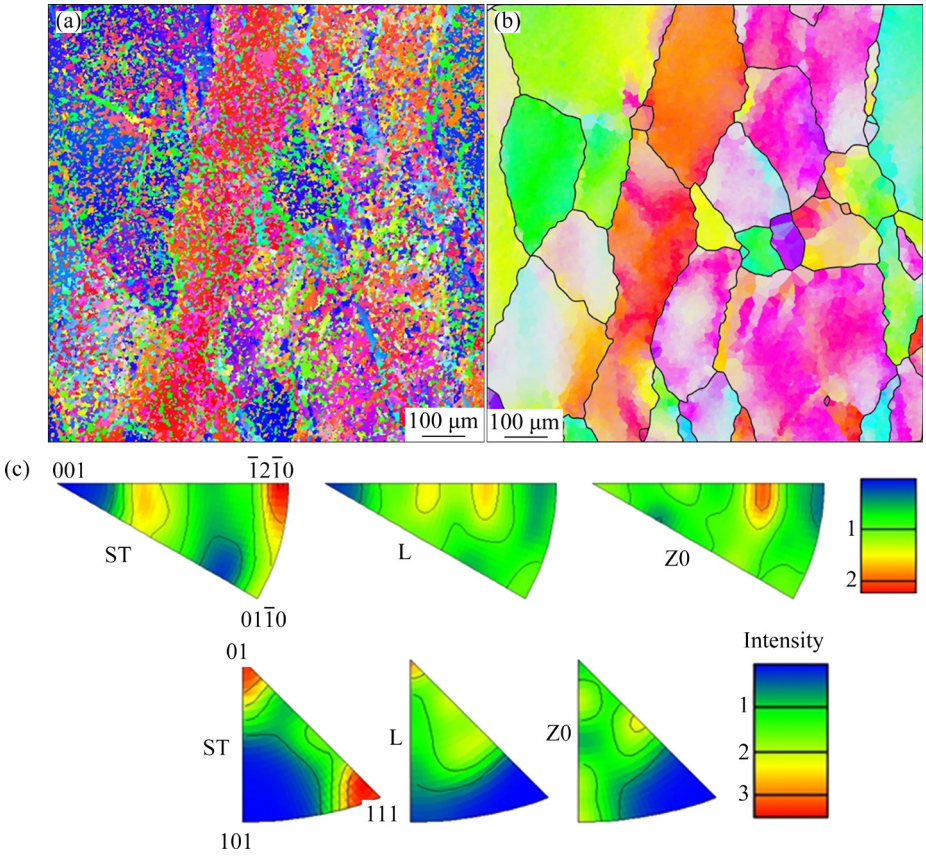

Fig. 17 (a) EBSD orientation map of S4 sample after heat treatment; (b) Reconstructed orientation and morphology of prior β grains; (c) IPF of α phase in S4 region

predominantly colored in red and blue. Figure 17(b) shows the reconstructed orientation and morphology details of the prior β grains derived from this analysis. The reconstructed data reveal that the prior β grains are elongated, with grain colors predominantly concentrated in the ⟨100⟩ and ⟨111⟩ orientations, which aligns with the observations in Section 3.2. Figure 17(c) depicts the inverse pole figure (IPF) calculated from the region shown in Fig. 17(a). As indicated in Fig. 8, it is evident that the generation of this texture is due to the strong ⟨111⟩ texture in the sample. As it is well known, the Burgers relationship in Ti alloys is $(110)_\beta//(0001)_\alpha$, $[1\,\bar{1}\,1]_\beta//[11\bar{2}0]_\alpha$. Therefore, in the S3 and S4 regions, the strong ⟨111⟩ texture will induce the formation of the $\{0001\}\langle 11\bar{2}0\rangle$ //ST fiber texture in the α phase.

4.3 Difference of mechanical properties in large strain region

In terms of impact toughness, the higher toughness observed in the L direction compared to the ST direction can be attributed to the morphology of the β grains in the samples [35,36]. Figure 18 shows the microstructure near the fracture surfaces of the specimens in the S4 region after the impact toughness test. In Figs. 18(a) and (b), crack in the L direction passes through the elongated β grains. During crack propagation, deflection repeatedly occurs due to the orientation differences between neighboring grains, thereby requiring higher energy absorption for crack propagation [37]. Conversely, in the ST direction, crack propagation is primarily perpendicular to the ST direction along β grain boundaries, which results in easy crack extension and consequently leads to inferior impact toughness (Figs. 18(c, d)). According to Table 3, impact toughness improves significantly in the L and LT directions with increasing strain. On the one hand, the prior β grains are elongated as strain increases. In samples S3 and S4, the crack traverses a greater number of β grains in the L and LT directions compared to S1 and S2. Therefore, the energy required for crack deflection within β grains is the highest in the S4 sample. Figure 19 depicts the schematic diagram of

the crack propagation path during impact toughness.

Furthermore, regarding tensile properties, the significant strength reduction in the ST direction is attributed to deformation texture. For S1 and S2 samples, considering their lower strain and the absence of pronounced texture, there is no significant difference in strength, with only a slight reduction in ductility observed in the ST direction. While as for the case of S3 and S4, a noticeable decrease in strength is linked to the development of β texture. The literature [38−40] shows that the elastic modulus of β phase in titanium alloy is 70−105 GPa, and the elastic modulus of α phase is 100−145 GPa. HÉMERY and VILLECHAISE [41] tested the elastic modulus of Ti-5553 alloy with different orientations and found that when the ⟨100⟩, ⟨101⟩, and ⟨111⟩ preferred orientations of β phase appear, the elastic moduli are 79, 92, and 97 GPa, respectively. Furthermore, HUET et al [42] demonstrated that when the loading direction is parallel to β grains with ⟨100⟩, ⟨111⟩, and ⟨101⟩ orientations, the β grains with ⟨100⟩ orientation experience premature plastic deformation. This is attributed to the lower stiffness of β grains along the ⟨100⟩ direction, leading to early elastic deformation.

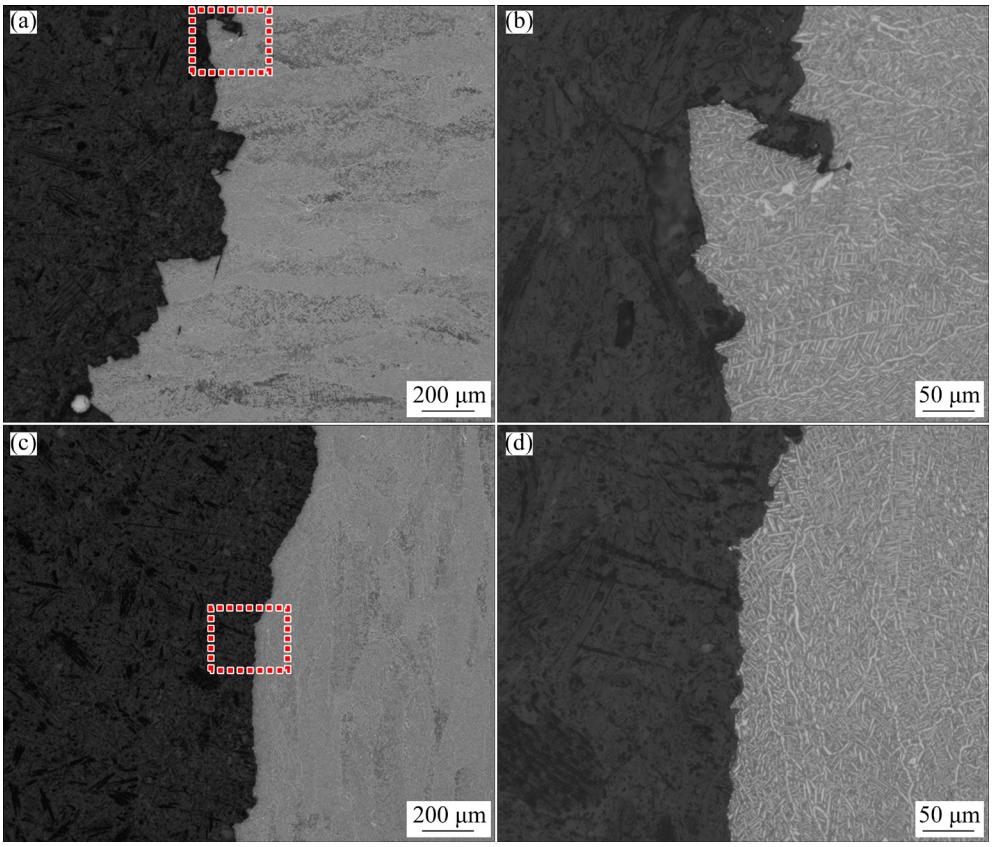

Fig. 18 Microstructures near fracture surfaces of specimens after impact toughness tests in S4 region: (a) Microstructure in L direction; (b) Enlarged figure of red box region in (a); (c) Microstructure in ST direction; (d) Enlarged figure of red box region in (c)

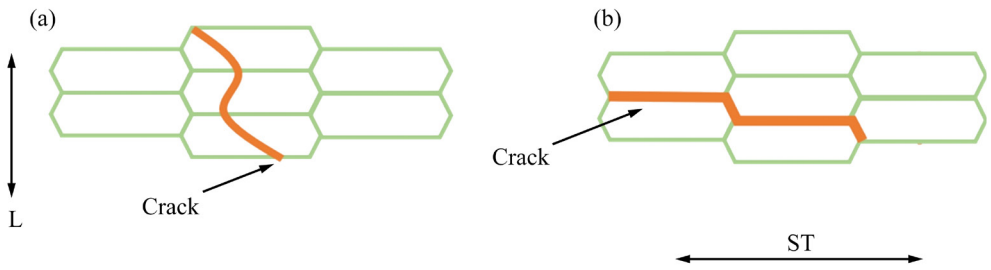

Fig. 19 Schematic diagrams of crack propagation path during impact toughness test along L (a) and ST (b) direction

Therefore, the difference in elastic modulus between the two phases leads to highly uncoordinated deformation, resulting in strain concentration. This phenomenon facilitates easier initiation and propagation of micro- cracks. Moreover, β grains oriented with ⟨100⟩ directions exhibit higher Schmid factors, making their slip systems more prone to activation. The study further indicates that the α phase embedded in β grains with ⟨100⟩ orientation experiences higher average stress levels compared to those embedded in β grains with ⟨101⟩ or ⟨111⟩ orientations. As a result, significant slip activity is primarily initiated in the β grains with ⟨100⟩ orientation [42]. Therefore, the development of ⟨100⟩ texture results in a significant reduction in UTS and El with increasing strain in Ti-55511 alloy die forgings.

In addition to the texture and morphology of the prior β grains, differences in mechanical properties are also influenced by the orientation of the α_p phase. When the loading direction is parallel to the c-axis, basal $\langle a\rangle$ slip $\{10\bar{1}0\}\langle 11\bar{2}0\rangle$ and prismatic $\langle a\rangle$ slip $\{10\bar{1}0\}\langle 11\bar{2}0\rangle$ are more difficult to activate [43]. At this stage, the α phase exhibits the highest elastic modulus and greater tensile strength. As the loading direction deviates from the c-axis, the initiation of basal $\langle a\rangle$ slip $\{10\bar{1}0\}\langle 11\bar{2}0\rangle$ and prismatic $\langle a\rangle$ slip $\{10\bar{1}0\}\langle 11\bar{2}0\rangle$ becomes easier, and the elastic modulus and tensile strength gradually decrease. For this reason, this paper counts the orientation of α_p within the white box region of Fig. 13(c), as illustrated in Fig. 20. The orientations of α_p can be categorized into two types. The first type is marked in red with a deviation angle of <30° along the c-axis. The second type is marked in blue with a deviation angle of <60°.

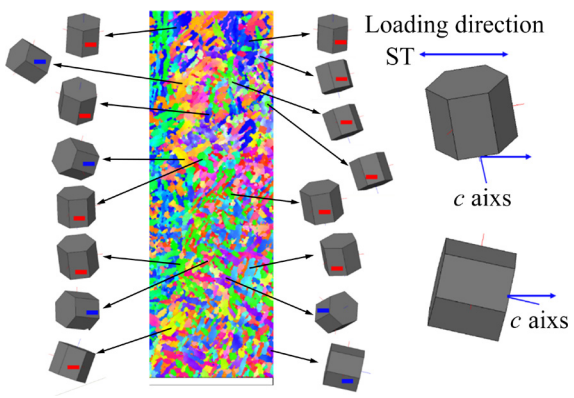

Fig. 20 Orientation distribution of different α-phase variants

It can be found that the number of α_p in the first type is much larger than that in the second type. When the loading direction is parallel to the ST direction, the loading force is nearly perpendicular to the c-axis of the first type of α_p phase and nearly parallel to the c-axis of the second type of α_p phase. Therefore, the basal $\langle a\rangle$ slip and prismatic $\langle a\rangle$ slip are easier to activate, leading to lower tensile strength. On the contrary, when the loading direction is parallel to the L direction, the basal $\langle a\rangle$ slip $\{0001\}\langle 11\bar{2}0\rangle$ and the prismatic $\langle a\rangle$ slip $\{10\bar{1}0\}\langle 11\bar{2}0\rangle$ are difficult to activate, resulting in higher strength.

To further verify the above inference, the Schmidt factors of basal $\langle a\rangle$ slip $\{0001\}\langle 11\bar{2}0\rangle$, prismatic $\langle a\rangle$ slip $\{10\bar{1}0\}\langle 11\bar{2}0\rangle$, and pyramidal $\langle a\rangle$ slip $\{10\bar{1}1\}\langle 11\bar{2}0\rangle$ are calculated for Fig. 12(L direction) and Fig. 13 (ST direction), as illustrated in Fig. 21. A higher Schmidt factor indicates that the slip is easier to activate. The results indicate that the Schmidt factor of the pyramidal $\langle a\rangle$ slip $\{10\bar{1}1\}\langle 11\bar{2}0\rangle$ is the highest when loaded in the L

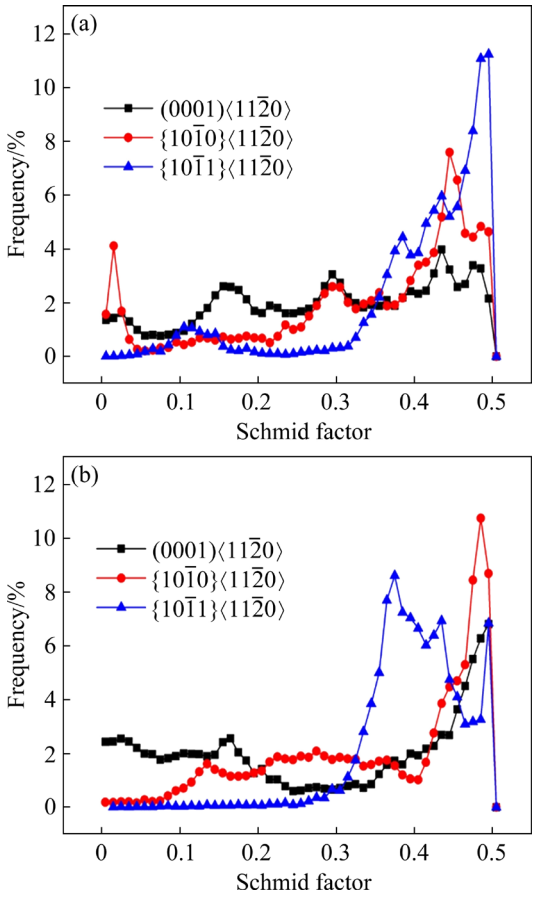

Fig. 21 Schmidt factor distribution of Ti-55511 alloy tensile sample with different slip systems: (a) L direction; (b) ST direction

direction. When the loading direction is parallel to the ST direction, the proportion of prismatic ⟨*a*⟩ slip $\{10\bar{1}0\}\langle 11\bar{2}0\rangle$ is the highest, followed by basal ⟨a⟩ slip $\{0001\}\langle 11\bar{2}0\rangle$. Therefore, when loading along the ST direction, the prismatic ⟨*a*⟩ slip $\{10\bar{1}0\}\langle 11\bar{2}0\rangle$ and the basal ⟨*a*⟩ slip $\{0001\}\langle 11\bar{2}0\rangle$ are preferentially activated, leading to reduced strength. When loading along the L direction, the small angle between the loading direction and the *c*-axis makes it difficult to activate prismatic ⟨*a*⟩ slip $\{10\bar{1}0\}\langle 11\bar{2}0\rangle$ and basal ⟨*a*⟩ slip $\{10\bar{1}0\}\langle 11\bar{2}0\rangle$, thereby increasing the strength. At the same time, the activation of prismatic ⟨*a*⟩ slip $(10\bar{1}0)\langle 11\bar{2}0\rangle$ further increases the strength.

According to the results of this study, and considering the actual deviation from the analysis of microstructure uniformity and mechanical properties, it can be determined that the strain in the forging process should be controlled to be less than 0.65 as far as possible. In the actual production, the deformation of forgings can be optimized by repeated iterations to weaken the texture and mechanical properties in different directions.

5 Conclusions

(1) The prior *β* grains are equiaxed in the small strain region, and the main deformation mechanism is DRV. The prior *β* grains are elongated in the large strain region, and the main deformation mechanisms are CDRX and DDRX.

(2) The {100} texture appears in the large strain regions (S3 and S4). Compared with S3, the texture intensity and volume fraction in the S4 region increase. As the strain increases, ⟨100⟩ oriented grains gradually expand, thereby enhancing the strength of the {100} texture. There is no significant difference in the thickness and volume fraction of the *α* phase after heat treatment in different strain regions.

(3) When the loading direction is parallel to the L direction, the strain is concentrated near the DRXed grains and inside the grains with ⟨100⟩ orientation, leading to crack initiation. When the loading direction is parallel to the ST direction, the strain is concentrated at the grain boundary of the grains with ⟨100⟩ orientation. At the same time, the crack occurs not only in the interior of the grain with ⟨100⟩ orientation but also at the grain boundary.

(4) Regarding impact toughness, the elongated prior *β* grains in the L direction enhance resistance to crack propagation. In terms of tensile properties, the difference in elastic modulus between the two phases causes highly uncoordinated deformation, leading to strain concentration, which makes the initiation and propagation of micro-cracks more likely.

CRediT authorship contribution statement

Heng-jun LUO: Investigation, Writing − Original draft, Formal analysis, Investigation; **Hao DENG:** Investigation, Formal analysis; **Wu-hua YUAN:** Conceptualization, Writing − Review & editing, Funding acquisition; **Wei XIANG:** Formal analysis; **Chang-min LI:** Investigation; **Wei-dong YIN** and **Hui YIN:** Methodology, Formal analysis; **Zou-yuan XU:** Formal analysis; **Sheng CAO:** Resources.

Declaration of competing interest

The authors declare that they have no known competing financial interests or personal relationships that could have appeared to influence the work reported in this paper.

Acknowledgments

This study was funded by Department of Science and Technology of Sichuan Province, China (No. 2022YFG0102), and the China Postdoctoral Science Foundation (No. 2023M733314).

References

[1] RAN Chun, SHENG Ze-min, CHEN Peng-wan, ZHANG Wang-feng, CHEN Qi. Effect of microstructure on the mechanical properties of Ti−5Al−5Mo−5V−1Cr−1Fe alloy [J]. Materials Science and Engineering: A, 2020, 773: 138728.

[2] COTTON J D, BRIGGS R D, BOYER R R, TAMIRISAKANDALA S, RUSSO P A, SHCHETNIKOV N, FANNING J C. State of the art in beta titanium alloys for airframe applications [J]. JOM, 2015, 67: 1281−1303.

[3] WEISS I, SEMIATIN S L. Thermomechanical processing of beta titanium alloys—An overview [J]. Materials Science and Engineering: A, 1998, 243: 46−65.

[4] SAUER C, LUETJERING G. Thermo-mechanical processing of high strength *β*-titanium alloys and effects on microstructure and properties [J]. Journal of Materials Processing Technology, 2001, 117: 311−317.

[5] PETERS M, KUMPFERT J, WARD C H, LEYENS C. Titanium alloys for aerospace applications [J]. Advanced Engineering Materials, 2003, 5: 419−427.

[6] QU F S, ZHOU Y H, ZHANG L Y, WANG Z H, ZHOU J.

Research on hot deformation behavior of Ti−5Al−5Mo−5V−1Cr−1Fe alloy [J]. Materials & Design, 2015, 69: 153−162.

[7] LIANG Hou-quan, GUO Hong-zhen, NING Yong-quan, PENG Xiao-na, QIN Chun, SHI Zhi-feng, NAN Yang. Dynamic recrystallization behavior of Ti−5Al−5Mo−5V−1Cr−1Fe alloy [J]. Materials & Design, 2014, 63: 798−804.

[8] LIANG Hou-quan, GUO Hong-zhen, NAN Yang, QIN Chun, PENG Xiao-na, ZHANG Jing-li. The construction of constitutive model and identification of dynamic softening mechanism of high-temperature deformation of Ti−5Al−5Mo−5V−1Cr−1Fe alloy [J]. Materials Science and Engineering: A, 2014, 615: 42−50.

[9] SHI Shuang-xi, LIU Xiu-sheng, ZHANG Xian-cheng, ZHOU Ke-chao. Comparison of flow behaviors of near beta Ti-55511 alloy during hot compression based on SCA and BPANN models [J]. Transactions of Nonferrous Metals Society of China, 2021, 31: 1665−1679.

[10] LI Kai, YANG Ping. The formation of strong {100} texture by dynamic strain-induced boundary migration in hot compressed Ti−5Al−5Mo−5V−1Cr−1Fe alloy [J]. Metals, 2017, 7: 412.

[11] SHI Shuang-xi, GE Jin-yang, LIN Yong-cheng, ZHANG Xian-cheng, ZHOU Ke-chao. High-temperature deformation behavior and recrystallization mechanism of a near beta titanium alloy Ti-55511 in β phase region [J]. Materials Science and Engineering: A, 2022, 847: 143335.

[12] LIM C V, LIU Yang, DING Chen, HUANG Ai-jun. Effect of supra-transus deformation conditions on recrystallization of beta Ti alloy [J]. Metals, 2021, 11: 1278.

[13] LIN Y C, HUANG Jian, LI Hong-bin, CHEN Dong-dong. Phase transformation and constitutive models of a hot compressed TC18 titanium alloy in the α+β regime [J]. Vacuum, 2018, 157: 83−91.

[14] SHI Xiao-hui, ZENG Wei-dong, SHI Chun-ling, WANG Hao-jun, JIA Zhi-qiang. The fracture toughness and its prediction model for Ti−5Al−5Mo−5V−1Cr−1Fe titanium alloy with basket-weave microstructure [J]. Journal of Alloys and Compounds, 2015, 632: 748−755.

[15] SHI Xiao-hui, ZENG Wei-dong, XUE Shi-kun, JIA Zhi-qiang. The crack initiation behavior and the fatigue limit of Ti−5Al−5Mo−5V−1Cr−1Fe titanium alloy with basket-weave microstructure [J]. Journal of Alloys and Compounds, 2015, 631: 340−349.

[16] BOYER R R. Attributes, characteristics, and applications of titanium and its alloys [J]. JOM, 2010, 62: 21−24.

[17] BEWLAY B P, GIGLIOTTI M F X, HARDWICKE C U, KAIBYSHEV O A, UTYASHEV F Z, SALISCHEV G A. Net-shape manufacturing of aircraft engine disks by roll forming and hot die forging [J]. Journal of Materials Processing Technology, 2003, 135: 324−329.

[18] SHEN G S, FURRER D. Manufacturing of aerospace forgings [J]. Journal of Materials Processing Technology, 2000, 98: 189−195.

[19] MAJILA A N, FERNANDO D C, BABU S N N, PATNAIK B V A, PRASAD N E. Evaluation of tensile properties and their correlation with microstructural characteristics of a closed die forging of iso-symmetrical aerospace grade Ti−6Al−4V alloy [J]. Defence Science Journal, 2015, 65: 171−178.

[20] GUPTA R K, KUMAR V A, KUMAR P R. Effect of variants of thermomechanical working and annealing treatment on titanium alloy Ti6Al4V closed die forgings [J]. Journal of Materials Engineering and Performance, 2016, 25: 2551−2562.

[21] SUÁREZ FERNÁNDEZ D, WYNNE B P, CRAWFORTH P, FOX K, JACKSON M. The effect of forging texture and machining parameters on the fatigue performance of titanium alloy disc components [J]. International Journal of Fatigue, 2021, 142: 105949.

[22] ZHANG Kun, ZHANG Kai, ZHU Yu-man, WU Xin-hua, WILLIAMS J, LIANG En-quan, MA Ji-sheng, ZHANG Ren, LIM C V S, HHUANG Ai-jun. Effect of deformation reduction on microstructure, texture, and mechanical properties of forged Ti−6Al−4V [J]. Journal of Materials Engineering and Performance, 2021, 30: 1147−1156.

[23] JIANG M G, YAN H, CHEN R S. Twinning, recrystallization and texture development during multi-directional impact forging in an AZ61 Mg alloy [J]. Journal of Alloys and Compounds, 2015, 650: 399−409.

[24] DENG Ying, ZHU Xin-wen, LAI Yi, GUO Yi-fan, FU Le, XU Guo-fu, HUANG Ji-wu. Effects of Zr/(Sc+Zr) microalloying on dynamic recrystallization, dislocation density and hot workability of Al−Mg alloys during hot compression deformation [J]. Transactions of Nonferrous Metals Society of China, 2023, 33: 668−682.

[25] CHEN Wen-xiong, HU Bao-jia, JIA Chun-ni, ZHENG Cheng-wu, LI Dian-zhong. Continuous dynamic recrystallization during the transient deformation in a Ni−30%Fe austenitic model alloy [J]. Materials Science and Engineering: A, 2019, 751: 10−14.

[26] CHEN Zhao-qi, XU Li-juan, CAO Shou-zhen, YANG Jian-kai, ZHENG Yun-fei, XIAO Shu-long, TIAN Jing, CHEN Yu-yong. Characterization of hot deformation and microstructure evolution of a new metastable β titanium alloy [J]. Transactions of Nonferrous Metals Society of China, 2022, 32: 1513−1529.

[27] HUANG Liang, LI Chang-min, LI Cheng-lin, HUI Song-xiao, YU Yang, ZHAO Ming-jie, GUO Shi-qi, LI Jian-jun. Research progress on microstructure evolution and hot processing maps of high strength β titanium alloys during hot deformation [J]. Transactions of Nonferrous Metals Society of China, 2022, 32: 3835−3859.

[28] YANG Jun-zhou, WU Jian-jun, XIE Hai-nan, LI Zhi-guo, WANG Kai-wei. Mechanism of continuous dynamic recrystallization of Ti−6Al−4V alloy during superplastic forming with sub-grain rotation [J]. Transactions of Nonferrous Metals Society of China, 2023, 33: 777−788.

[29] BECK P A, SPERRY P R. Strain induced grain boundary migration in high purity aluminum [J]. Journal of Applied Physics, 1950, 21: 150−152.

[30] LU Tong, DAN Zhen-hua, LI Kai, YI Dan-qing, ZHOU Lian, CHANG Hui. Hot deformation behaviors and dynamic recrystallization mechanism of Ti-35421 alloy in β single field [J]. Transactions of Nonferrous Metals Society of China, 2022, 32: 2889−2907.

[31] LI L, LUO J, YAN J J, LI M Q. Dynamic globularization and restoration mechanism of Ti−5Al−2Sn−2Zr−4Mo−4Cr alloy during isothermal compression [J]. Journal of Alloys and

Compounds, 2015, 622: 174−183.
[32] LI Chang-min, HUANG Liang, ZHAO Ming-jie, GUO Shi-qi, SU Yang, LI Jian-jun. Systematic analysis of the softening mechanism and texture evolution of Ti−6Cr−5Mo−5V−4Al alloy during hot compression in $\alpha+\beta$ phase region [J]. Materials Science and Engineering: A, 2022, 850: 143571.
[33] ZHANG Yu-qin, CHENG Wei-li, YU Hui, WANG Hong-xia, NIU Xiao-feng, WANG Li-fei, LI Hang. Unveiling the twinning and dynamic recrystallization behavior and the resultant texture evolution in the extruded Mg−Bi binary alloys during hot compression [J]. Journal of Materials Science & Technology, 2022, 105: 274−285.
[34] PRIMIG S, LEITNER H, KNABL W, LORICH A, CLEMENS H, STICKLER R. Textural evolution during dynamic recovery and static recrystallization of molybdenum [J]. Metallurgical and Materials Transactions A, 2012, 43: 4794−4805.
[35] PETERS J O, LÜTJERING G. Comparison of the fatigue and fracture of $\alpha+\beta$ and β titanium alloys [J]. Metallurgical and Materials Transactions A, 2001, 32: 2805−2818.
[36] LÜTJERING G, ALBRECHT J, SAUER C, KRULL T. The influence of soft, precipitate-free zones at grain boundaries in Ti and Al alloys on their fatigue and fracture behavior [J]. Materials Science and Engineering: A, 2007, 468/469/470: 201−209.
[37] CHEN Wei, ZENG Wei-dong, WANG Bo-shuai, XU Jian-wei. Fracture toughness anisotropy of Ti17 disk fabricated by through-transus-processed forging and the role of toughening mechanisms [J]. Materials Science and Engineering: A, 2023, 881: 145441.
[38] WELSCH G, BOYER R, COLLINGS E. Materials properties handbook: Titanium alloys [M]. Materials Park, Ohio: ASM International, 1994.
[39] LÜTJERING G, WILLIAMS JC, GYSLER A. Microstructure and mechanical properties of titanium alloys [M]. Singapore: World Scientific Publishing Company, 2000.
[40] ZARKADES A, LARSON F R. Elasticity of titanium sheet alloys [M]//The Science, Technology, and Application of Titanium. Oxford: Pergamon Press, 1970: 933−941.
[41] HÉMERY S, VILLECHAISE P. Influence of β anisotropy on deformation processes operating in Ti−5Al−5Mo−5V−3Cr at room temperature [J]. Acta Materialia, 2017, 141: 285−293.
[42] HUET A, NAÏT-ALI A, GIROUD T, VILLECHAISE P, HÉMERY S. Onset of plastic deformation and strain localization in relation to β phase in metastable β and dual phase Ti alloys [J]. Acta Materialia, 2022, 240: 118348.
[43] WON J W, PARK K T, HONG S G, LEE C S. Anisotropic yielding behavior of rolling textured high purity titanium [J]. Materials Science and Engineering: A, 2015, 637: 215−221.

截面变化对 Ti-55511 合金大型模锻件准 β 锻造显微组织和性能的影响

罗恒军[1,2]，邓 浩[2]，袁武华[1]，向 伟[1,2]，李昌民[2]，尹卫东[2]，尹 慧[2]，徐邹圆[2]，曹 晟[3]

1. 湖南大学 材料科学与工程学院，长沙 410082；
2. 中国第二重型机械集团 德阳万航模锻有限责任公司，德阳 618013；
3. 暨南大学 化学与材料学院 先进耐磨蚀与功能材料研究所，广州 510632

摘 要：通过设计台阶状模锻件，研究 Ti−5Al−5Mo−5V−1Cr−1Fe (Ti-55511)合金在不同应变下的显微组织和性能。结果表明，在大应变区发生连续动态再结晶(CDRX)和非连续动态再结晶(DDRX)。CDRX 产生的颗粒取向是随机的，不会弱化纤维织构。随着应变的增加，⟨100⟩取向的晶粒逐渐扩展进而提高了{100}织构强度。大应变区域的力学性能表现出明显的各向异性。原位拉伸实验表明，当加载方向与纵向(L)平行时，应变集中在动态再结晶晶粒附近和⟨100⟩取向的晶粒内部，导致裂纹萌生。此外，由于加载方向与 c 轴夹角较小，很难激活柱面滑移和基面滑移，从而提高了强度。当加载方向与高向(ST)平行时，裂纹不仅在⟨100⟩取向晶粒内部产生，而且还在晶界处产生。在冲击韧性方面，L 方向的“扁平”β 晶粒提高了抗裂纹扩展能力。

关键词：Ti−5Al−5Mo−5V−1Cr−1Fe 合金；台阶状模锻件；应变分布；变形机制；力学性能

(Edited by Xiang-qun LI)